Accepted Manuscript

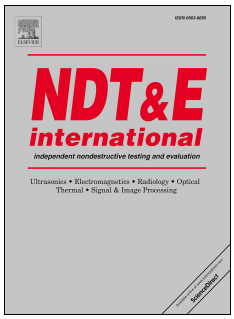

In-plane local defect resonances for efficient vibrothermography of impacted carbon fiber-reinforced composite (CFRP)

Joost Segers, Saeid Hedayatrasa, Erik Verboven, Gaétan Poelman, Wim Van Paepegem, Mathias Kersemans

PII: S0963-8695(18)30398-0

DOI: https://doi.org/10.1016/j.ndteint.2018.12.005

Reference: JNDT 2067

To appear in: *NDT and E International*

Received Date: 11 July 2018

Revised Date: 8 October 2018

Accepted Date: 14 December 2018

Please cite this article as: Segers J, Hedayatrasa S, Verboven E, Poelman Gaé, Van Paepegem W, Kersemans M, In-plane local defect resonances for efficient vibrothermography of impacted carbon fiber-reinforced composite (CFRP), *NDT and E International* (2019), doi: https://doi.org/10.1016/j.ndteint.2018.12.005.

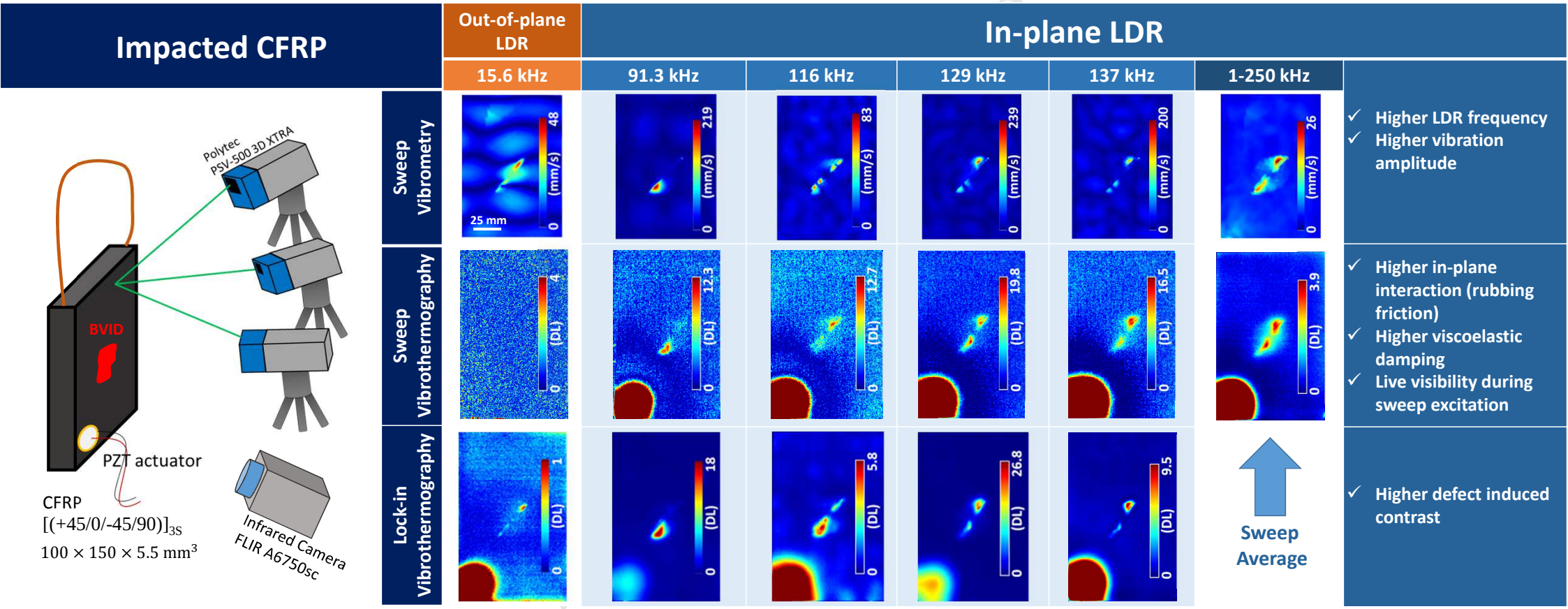
Impacted CFRP
Out-of-plane LDR
In-plane LDR
15.6 kHz
91.3 kHz
116 kHz
129 kHz
137 kHz
1-250 kHz
Sweep Vibrometry
Sweep Vibrothermography
Lock-in Vibrothermography
Polytec PSV-500 3D XTRA
BVID
PZT actuator
CFRP
[(+45/0/-45/90)]3S
100 × 150 × 5.5 mm3
Infrared Camera FLIR A6750sc
25 mm
(mm/s)
(DL)
Sweep Average
✓ Higher LDR frequency
✓ Higher vibration amplitude
✓ Higher in-plane interaction (rubbing friction)
✓ Higher viscoelastic damping
✓ Live visibility during sweep excitation
✓ Higher defect induced contrast

In-plane Local Defect Resonances for Efficient Vibrothermography of Impacted Carbon Fiber-Reinforced Composite (CFRP)

Joost Segers[1], Saeid Hedayatrasa[1,2], Erik Verboven[1], Gaétan Poelman[1,2], Wim Van Paepegem[1] and Mathias Kersemans[1,#]

[1] Department of Materials, Textiles and Chemical Engineering, Ghent University, Technologiepark-Zwijnaarde 903, B-9052 Zwijnaarde, Belgium

[2] SIM Program M3 DETECT-IV, Technologiepark-Zwijnaarde 935, B-9052 Zwijnaarde, Belgium

[#] Corresponding author

ABSTRACT

It is well known that the efficiency of the vibrothermographic non-destructive testing (NDT) technique can be enhanced by taking advantage of local defect resonance (LDR) frequencies. Recently, the classical out-of-plane local defect resonance was extended towards in-plane LDR for enhanced efficiency of vibrometric NDT. This paper further couples the concept of this in-plane LDR to vibrothermography, on the basis of the promising potential of in-plane LDRs to enhance the rubbing (tangential) interaction and viscoelastic damping of defects. Carbon fiber-reinforced composites (CFRPs) with barely visible impact damage (BVID) are inspected and the significant contribution of in-plane LDRs in vibrational heating is demonstrated. Moreover, it is shown that the defect thermal contrast induced by in-plane LDRs is so high that it allows for easy detection of BVID by live monitoring of infrared thermal images during a single broadband sweep excitation. Thermal and vibrational spectra of the inspected surface are studied and the dominant contribution of in-plane LDR in vibration-induced heating is demonstrated.

KEYWORDS: In-plane local defect resonance (LDR_{XY}); Vibrothermography; Non-destructive testing (NDT); Composite materials; BVID.

1. Introduction

Composite materials such as carbon fiber reinforced polymer (CFRP) are widely used in many advanced engineering structures for their high specific strength and their resistance to fatigue and corrosion. Due to the layered material structure, composites are susceptible to a wide variety of (internal) damages. A well-known example is the complex distribution of cracks and delaminations resulting from a low velocity impact, which is commonly referred to as barely visible impact damage (BVID).

Vibrothermography (also referred to as thermosonics or sonic thermography) is a non-destructive testing (NDT) technique which takes advantage of vibrational energy dissipation at defects subjected to a dynamic stimulation. As such, the defects behave like localized heat sources and can be detected with a thermographic system [1]. This makes vibrothermography a promising technique for detection of tightly closed cracks and kissing bonds in composites, especially if the defect interfaces are aligned normal to the inspection surface which is hard to detect using other NDT techniques [2].

High power ultrasonic horns and transducers are often used in classical vibrothermography in order to properly activate the defects and to increase the vibrational heating to a detectable level [3, 4]. The required high power imposes practical difficulties (i.e. need for a high power supply and relevant hardware requirements) and has to be limited in order to prevent component degradation by the excitation source itself. Recently, alternative low power vibrothermography techniques were introduced by taking advantage of the high amplitude vibrations at global or local resonances. In so called self-heating based vibrothermography [5, 6] the fundamental global modal frequencies of the test piece are used as the excitation frequency. An electrodynamic shaker is used to stimulate global resonation of the test piece at a particular modal frequency or a combination of modal frequencies (normally less than 1000 Hz). This approach is shown to boost the global heating of the specimen induced by vibrational damping which indicates distinct gradients at the defected areas.

Another low power vibrothermography alternative is based on the concept of local defect resonance (LDR) for enhanced efficiency [7, 8]. The excitation at LDR frequencies allows for selective resonation of the defect's features by using low power piezoelectric actuators [9]. Generally, the component is excited at an LDR frequency of the defect and the corresponding vibration induced heat is diffused to the surface and detected using a high-sensitivity infrared camera [10-15]. The efficiency of LDR based vibrothermography can be enhanced through nonlinear ultrasound spectroscopy and selecting those LDR frequencies that indicate highest amplitudes of defect induced second harmonics [16-18]. Furthermore, applying a combination of an LDR and a modulation frequency that shows highest side band amplitudes (so called nonlinear wave modulation thermography) intensifies the defect's interaction with excited vibrations and raises the resultant heating [19].

Various vibrational heating mechanisms can be activated through LDR, depending on the orientation, asperities and the gap or tightness of the defect's interfaces [20-22]. LDR induced interactions of the defect's interfaces dissipate heat by rubbing friction and adhesion hysteresis at closures [20, 21]. Moreover, LDR induced deformation of the defect's features dissipates heat through viscoelastic damping, thermoelastic damping

and plastic deformation [20-22]. The latter source may come to effect at a too large excitation power and must be avoided due to its destructive nature.

Consequently, the polarization of LDR oscillations with respect to the defect's orientation has considerable impact on its detectability and the relative contribution of heating mechanisms. Different LDR mode shapes may have dominant out-of-plane polarization (i.e. normal to the inspection surface) or dominant in-plane polarization (i.e. parallel to the inspection surface) corresponding to the different features of the defected area. However, traditionally LDR was known as, and evidenced by, out-of-plane local defect resonance (LDR_z) behavior until recently that the current authors introduced in-plane local defect resonance (LDR_{XY}) [23] and showed its efficiency in vibrometric NDT. Among the results presented in [23], it was shown that a CFRP coupon with BVID shows clear LDR_{XY} response which reveals distinct damage features that are not present in the LDR_z behavior. It is also shown that, due to high in-plane stiffness of laminas, LDR_{XY} is generally excited at higher frequencies compared to LDR_Z.

An LDR_Z dominantly stimulates normal interaction of the defect's interfaces and dissipates heat through adhesion and partial rubbing of touching asperities [21]. On the contrary, an LDR_{XY} leads to dominant tangential interaction (full rubbing) of in-plane interfaces e.g. delamination (Figure 1(b)) as well as through-the-thickness interfaces e.g. matrix cracks (Figure 1(a)) and fiber breakages. Therefore, it is expected that LDR_{XY} is more effective than LDR_Z in terms of frictional heating at closures, as schematically shown in Figure 1. Moreover, LDR_{XY} frequencies are generally higher than LDR_Z frequencies which naturally lead to increased viscoelastic and frictional dissipation [24].

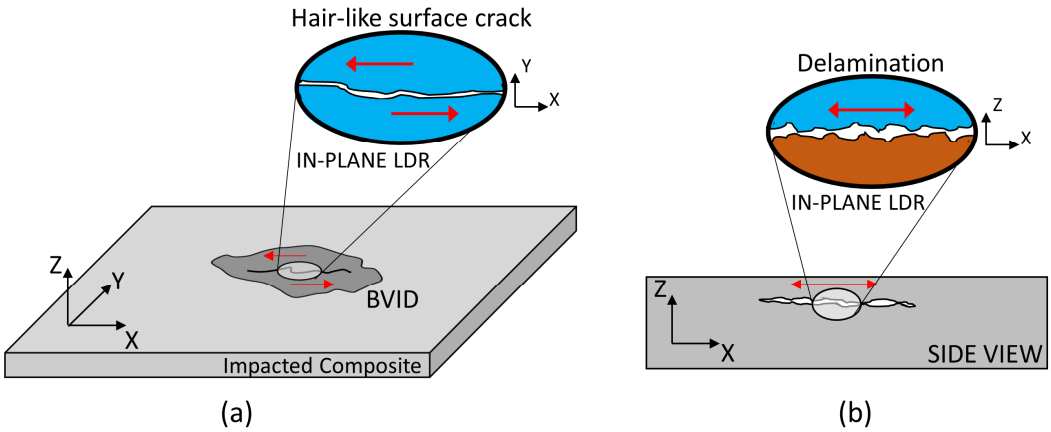

Figure 1. Schematic representation of dominant tangential interaction at in-plane LDR for (a) out-of-plane surface crack interfaces and (b) in-plane delamination interfaces of a typical impact damage in a CFRP sample.

This experimental study investigates the contribution of LDR_{XY} in vibrational heating of BVID in CFRP specimens compared to LDR_Z. A 3D infrared scanning laser Doppler vibrometer (SLDV) is used to record the specimen's vibrations and to identify the out-

of-plane and in-plane LDR frequencies. A cooled infrared camera is used to measure the vibrational heating induced at the BVID when subjected to the identified LDR frequencies.

2. Material and methods

The vibrational and corresponding thermal responses are evaluated for two $100 \times 150 \times 5.5$ mm^3 CFRP coupons. The samples are manufactured out of 24 layers of unidirectional carbon fiber according to a cross-ply $[(0/90)]_{6s}$ and a quasi-isotropic $[(+45/0/-45/90)]_{3s}$ lay-up. Both samples were impacted with a 7.1 kg drop-weight from a height of 0.1 m according to the ASTM D7136 [25]. The impact energy was measured 6.3 J, which introduced the BVID. Both samples are shown in Figure 2 together with the corresponding C-scan amplitude and time-of-flight (TOF) images, showing the complex damage distribution at the impact location. The C-scan results are obtained in reflection mode using dynamic time gating [26]. A focused transducer at 5 MHz (H5M, General Electric) is employed. Both samples display a hair-like surface crack at the backside resulting from the low velocity impact. A microscopic view of this crack is shown in the inset of Figure 2(g) for the cross-ply coupon.

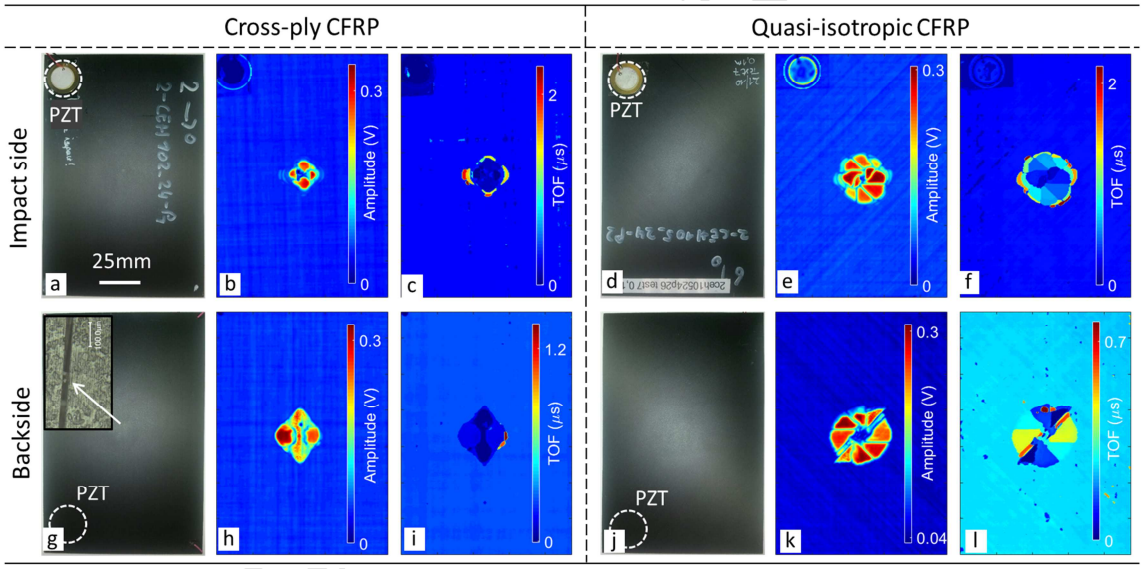

Figure 2. CFRP test specimens with BVID and corresponding C-scan amplitude and TOF images: (a-c , g-i) Cross-ply $[(0/90)]_{6s}$, and (d-f , j-l) Quasi-isotropic $[(+45/0/-45/90)]_{3s}$.

For vibrational studies, each sample is excited using a low power piezoelectric (PZT) patch (type EPZ-20MS64W from Ekulit, with a diameter of 12 mm) glued to its impact side. A sweep excitation from 1 to 250 kHz is used together with a Falco System WMA-300 voltage amplifier to increase the excitation voltage to 150 V_{pp}. The resulting electrical power supplied to the actuator is in the order of a few Watt. The broadband in-plane and out-of-plane vibrational response is measured using a 3D infrared scanning laser Doppler vibrometer (Polytec PSV-500-3D XTRA).

BVID is a complex type of damage [27] and previous studies of the authors have shown that this results in LDR_Z and LDR_{XY} behavior of different parts of the damaged area at

distinct frequencies [23, 28]. In this study, the LDR_Z and LDR_{XY} frequencies are extracted manually from the acquired frequency spectra by analysis of the operational deflection shapes for the most prominent LDR behavior. Alternatively, advanced post-processing algorithms [29] are under development to extract them in an automated manner.

Several extracted LDR frequencies are examined by lock-in vibrothermography (LVT) with a modulation frequency of 0.05 Hz for two cycles in order to enhance the signal-to-noise ratio (SNR) [30]. Alternatively, a sweep vibrothermography (SVT) experiment is performed with a linear sweep excitation from 1 to 250 kHz for 50 s. The vibrational heating is measured by a FLIR A6750sc infrared camera (controlled by *edevis GmbH* hardware-software), which has a cryo-cooled InSb detector with a pixel density of 640 x 512 pixels, a noise equivalent differential temperature (NEDT) of < 20 mK and a bit depth of 14 bit. For the excitation of the PZTs, a function generator is used together with the Falco amplifier to apply the excitation voltage of 150 V_{pp} for all experiments. The thermograms are measured at a sampling rate of 125 Hz and post-processed by fast Fourier transform (FFT) to extract corresponding amplitude and phase images in case of LVT. For SVT, live thermal images corresponding to the LDR frequencies and thermal spectra corresponding to the entire sweep frequency range are studied.

3. Results and Discussion

3.1 Lock-in vibrothermography (LVT) of impacted cross-ply CFRP

The experimental results at LDR frequencies corresponding to the impact side and backside of the cross-ply $[(0/90)]_{6s}$ CFRP sample (see Figure 2(a)) are respectively summarized in Figure 3 and Figure 4. The top row corresponds to the SLDV measurements, the middle row to the amplitude of LVT measurements, and the bottom row to the phase images of the LVT measurements. The SLDV images show the combined in- and out-of-plane velocity amplitude for the arbitrary frequency, the out-of-plane velocity component for the LDR_Z and the in-plane velocity component for the LDR_{XY}. The LVT amplitude images are presented in digital level (DL) scale, which is the raw output measured by the infrared camera, and which thus corresponds to the intensity of emitted infrared radiation. The limits of the color maps of the LVT images are set to the extreme values at the defected area and its surrounding sound area. In this way the colormap scale defines the defect induced thermal contrast (DTC) regardless of the heating induced by the PZT itself.

The manually selected LDR frequencies are indicated in the figure. In addition, an arbitrary frequency of 95 kHz is also examined to emphasize the dominant contribution of LDR in vibrational heating.

3.1.1 Impact side

According to Figure 3(a-g), the impact side of the cross-ply sample indicates three LDR_Z in the lower frequency range 23.5-54.5 kHz and three LDR_{XY} in the higher frequency range 133-174 kHz. The arbitrary frequency of 95 kHz indicates a very small DTC of 0.6 DL in the amplitude image (Figure 3(h)) corresponding to the relatively small increased vibrational activity at the defect as shown in its combined in- and out-of-plane velocity map (Figure 3(a)). Regarding LDRs, except for the fundamental LDR_Z at 23.5 kHz, all others are detected by LVT in both amplitude and phase images. The agreement of the velocity maps and the thermal signature of the LDRs is excellent and there are minor blurring effects induced by the 3D anisotropic heat diffusion. Moreover, the higher global damping induced at relatively high frequencies of LDR_{XY} leads to thermal traces of the global mode shapes in corresponding amplitude and phase images. This can be seen on the amplitude image of LDR_{XY} at 133 kHz (Figure 3(L)) which is strongly affected by the global heating due to resonation of its upper edge. The global heating and the in-plane heat flow induced by the PZT are more pronounced in the phase images, because they indicate the phase delay of the thermal evolution at each individual pixel regardless of the absolute temperature. Therefore, phase images are generally more noisy than amplitude images.

The fundamental LDR_Z at 23.5 kHz is not detected through LVT (Figure 3(i)) while the other two LDR_Z at 35.2 and 54.5 kHz are indicated with a DTC of 1.9 and 1.2 DL respectively. This indicates that the normal interaction of relevant defect interfaces cannot heat the defect to a detectable limit at the relatively low out-of-plane velocity of 22 mm/s corresponding to this fundamental LDR_Z. However, the LDR_{XY} at 133, 151 and 174 kHz are detected with higher DTC compared to the LDR_Z, equal to 3.2, 7.1 and 3.5 DL respectively (see also Table 1).

Although higher LDR velocity implies increased viscoelastic and frictional energy dissipation, other factors e.g. depth, orientation, gap and morphology of asperities of relevant interfaces also affect the vibrational heating and therefore the measured DTC. This argument can explain why the DTC of LDR_Z at 35.2 kHz is higher compared to the DTC of LDR_Z at 54.5 kHz, despite its lower out-of-plane velocity and smaller size. Likewise, the DTC of LDR_{XY} at 174 kHz with in-plane velocity of 56 mm/s is higher than the one at 133 kHz with in-plane velocity of 121 mm/s.

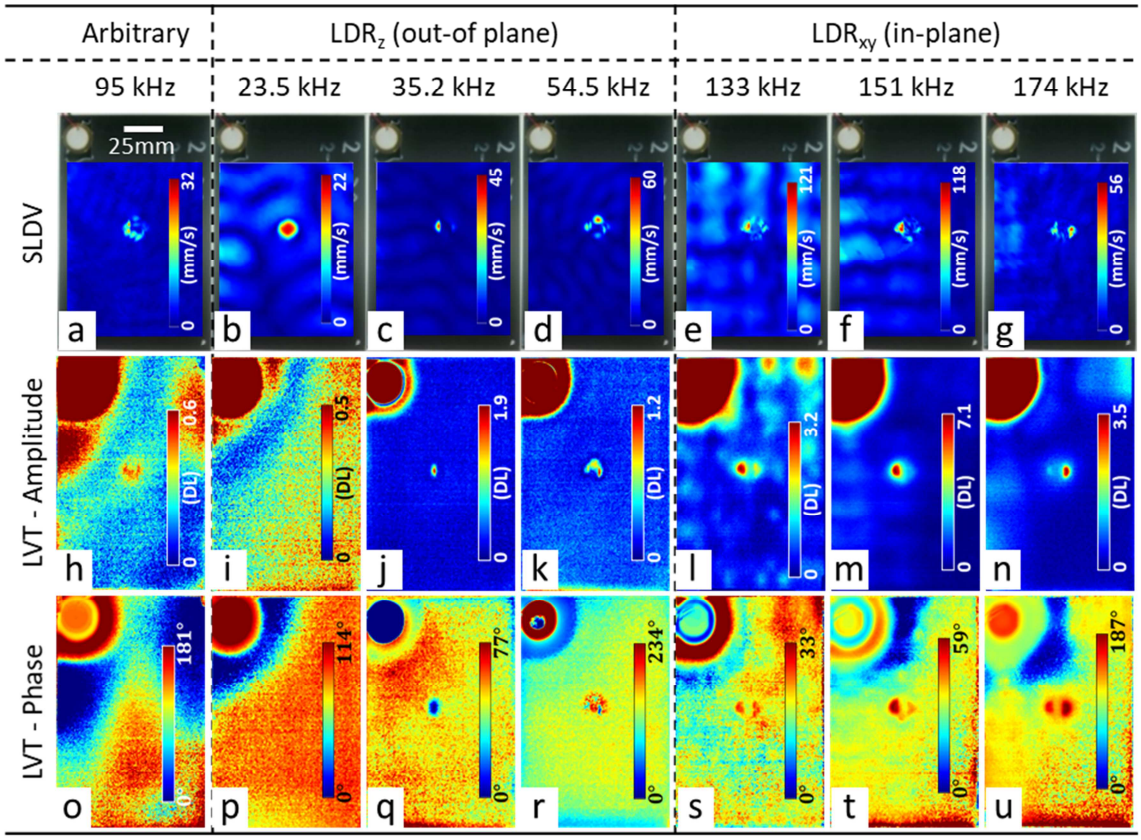

Figure 3. Measurements corresponding to the impact side of the cross-ply $[(0/90)]_{6s}$ CFRP sample: (a-g) amplitude of vibration, (h-n) amplitude of LVT and (o-u) phase of LVT.

3.1.2 Backside

The measurements corresponding to the backside of the cross-ply sample (see Figure 4) also indicate three LDR_Z in the frequency range 17.2-109 kHz and three LDR_{XY} in the frequency range 82.9-142 kHz. There is a hair-like surface crack (see inset of Figure 1(g)) at the center of the defect in the backside of this sample which dominantly affects its LDR behavior. The arbitrary frequency of 95 kHz barely shows a trace of the defect in the corresponding LVT images, while stimulation at the various LDR frequencies show clear signals in both amplitude and phase LVT images.

Among LDR_Z, the one at 17.2 kHz with an out-of-plane velocity of 40 mm/s leads to the highest DTC of 1.3 DL. According to the corresponding velocity map (see Figure 4(b)), this is the fundamental LDR_Z of the defect leading to tangential interaction of the interfaces along the hair-like surface crack. The other two LDR_Z at higher frequencies 49.6 and 109 kHz lead to lower DTC of 0.5 and 0.9 DL despite their higher LDR velocities. The corresponding velocity maps (see Figure 4(c,d)) indicate that these LDR_Z (particularly the one at 109 kHz) are comprised of a cluster of relatively smaller subsurface features spread over the defect area. These are dominantly in-plane interfaces with normal interaction and/or deeper defect features, leading to lower vibrational heating compared to the fundamental LDR at 17.2 kHz. Moreover, the

amplitude image of the LDR_Z at 109 kHz is influenced by a global in-plane mode shape of the plate (see Figure 4(k)). The out-of-plane vibration response (Poisson effect) of this in-plane mode shape is visible in Figure 4(d).

Furthermore, the LDR_{XY} at 98.9 and 142 kHz, with maximum in-plane velocities of 126 and 165 mm/s (Figure 4(f,g)), indicate defect features with very high DTC of 14.6 and 12.9 DL (Figure 4(m,n)) respectively. The DTC of the lowest LDR_{XY} at 82.9 kHz is 0.6 DL (Figure 4(L)) which is relatively low due to the corresponding low in-plane velocity of 41 mm/s (Figure 4(e)). As mentioned earlier, other factors might contribute to the low DTC of this LDR_{XY} like a too loose gap of relevant interfaces which reduces their tangential interaction and/or a deeper depth of relevant features that diffuses the defect's thermal signature.

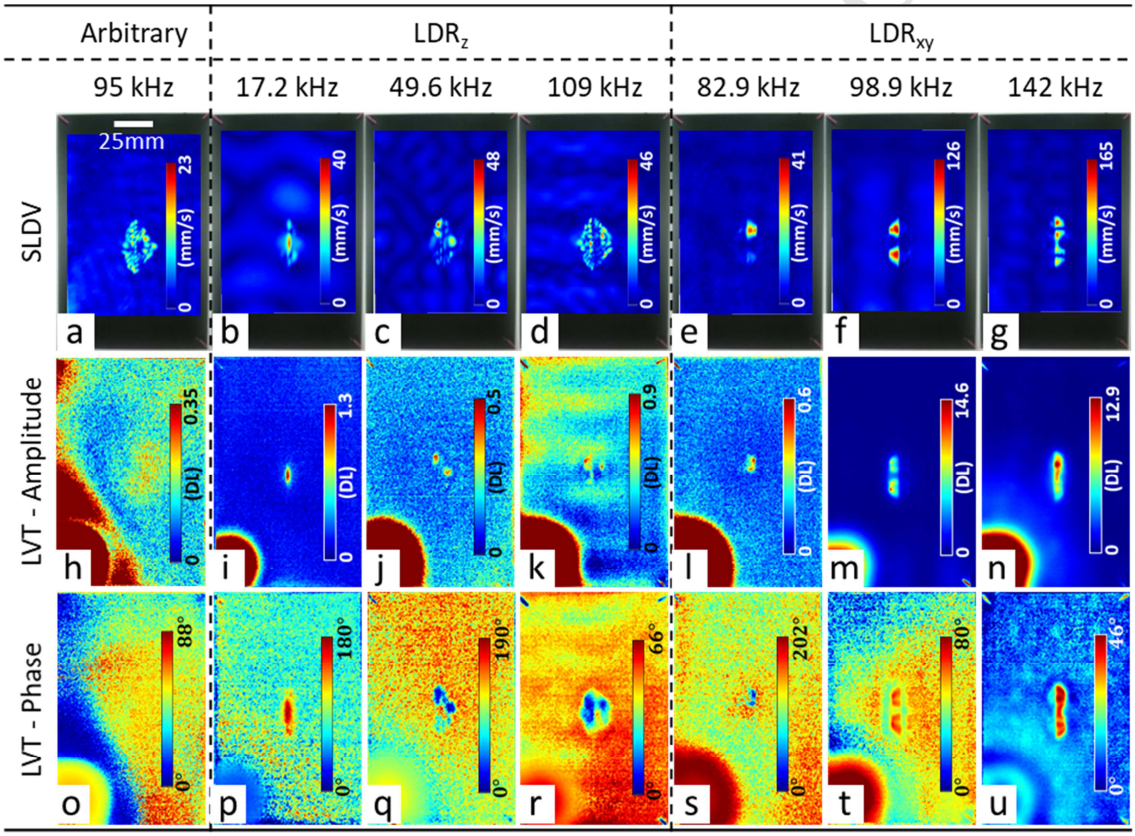

Figure 4. Measurements corresponding to the backside of the cross-ply $[(0/90)]_{6s}$ CFRP sample: (a-g) amplitude of vibration, (h-n) amplitude of LVT and (o-u) phase of LVT.

3.1.3 Overview of the results

All measured DTCs of the impacted cross-ply CFRP are summarized in Table 1. Comparing the DTCs of the examined LDR frequencies evidently confirms the higher DTC (i.e. detectability) of LDR_{XY} when inspecting BVID, either from the impact side or from the backside. It is noteworthy that the DTC of 0.5 at the fundamental LDR_Z at 23.5 kHz (Figure 3(i)) is just an indication of the noise level and provides no defect contrast.

Table 1. Summary of DTCs measured for the impact side (Figure 3(h-n)) and the backside (Figure 4(h-n)) of the cross-ply $[(0/90)]_{6s}$ CFRP.

$[(0/90)]_{6S}$ CFRP	Parameter	Arbitrary	LDR_Z			LDR_{XY}		
Impact side	f (kHz)	95	23.5	35.2	54.5	133	151	174
	DTC (DL)	0.6	0.5	1.9	1.2	3.2	7.1	3.5
Backside	f (kHz)	95	17.2	49.6	109	82.9	98.9	142
	DTC (DL)	0.35	1.3	0.5	0.9	0.6	14.6	12.9

The defect features detected by LVT at different LDR frequencies are in good agreement with those areas having relatively low TOFs in the C-scan images (i.e. shallow features): the left and right inner lobes at the impact side (Figure 2(c)) and the two left and right lobes at the backside (Figure 2(i)). Deeper damage features including the outer peripheral features of the impact side (Figure 2(b,c)) and the left and right lobes of the backside (Figure 2(h,i)) are missing in the corresponding SLDV and LVT results. Further investigation needs to be done to address these limitations: (i) the capability of LDR based NDT for detecting such deep features (which are expected to show LDR behavior at higher frequency ranges), and (ii) evaluating the capability of LVT to adequately excite these deep features and detect their diffused thermal signature.

3.2 Sweep vibrothermography (SVT) of impacted Quasi-isotropic CFRP

To further evaluate the potential of LDR_{XY} in vibrothermography, the CFRP sample with quasi-isotropic layup $[(+45/0/-45/90)]_{3s}$ is inspected from the backside (Figure 2(j)). First, the thermal and vibrational results are presented at LDR frequencies (see Figure 5). Subsequently, the spectra corresponding to the entire sweep frequency range are studied (see Figure 6 and Figure 7).

3.2.1 LDR frequency response

From the SLDV measurements, the following frequencies have been selected for further investigation: the arbitrary frequency of 95 kHz, the fundamental LDR_Z at 15.6 kHz and four LDR_{XY} in the frequency range 91.3-137 kHz. The top row of Figure 5 shows the SLDV measurements, the middle row the SVT measurements and the bottom row the LVT measurements (to validate the SVT measurements) at these frequencies. Similar to Figure 3 and Figure 4, the SLDV images (Figure 5(a-f)) show the combined in- and out-

of-plane velocity amplitude for the arbitrary frequency, the out-of-plane velocity component for the LDR_Z and the in-plane velocity component for the LDR_{XY}. Moreover, the combined in- and out-of-plane velocity amplitude is averaged over the whole sweep excitation as shown in Figure 5(g). From the results it is clear that the vibrometric behavior of this impact damage is significantly influenced by the hair-like surface crack along the fibers and the two adjacent triangle-like delaminations closest to the surface (see also Figure 1(l)).

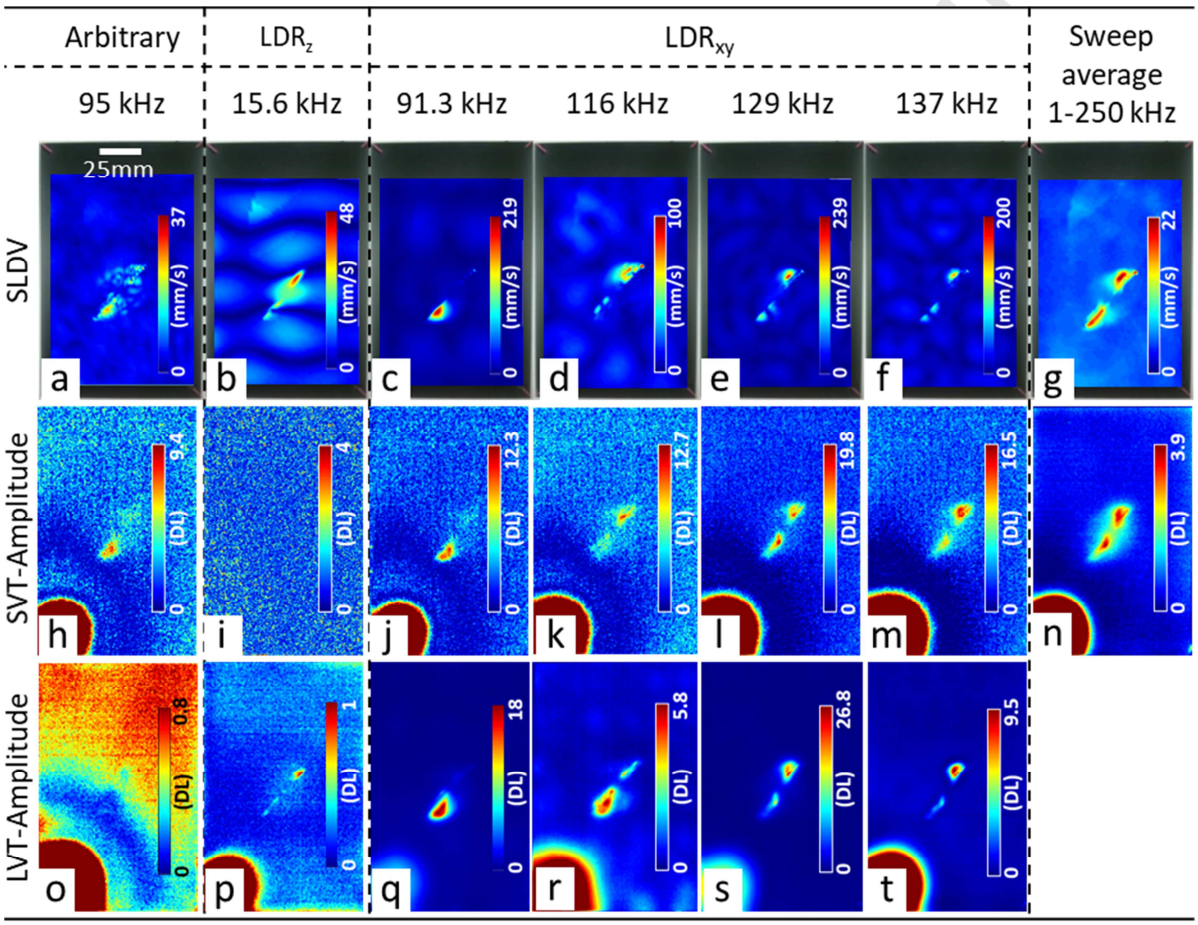

Figure 5. Measurements corresponding to the backside of the quasi-isotropic $[(+45/0/-45/90)]_{3s}$ CFRP sample: (a-g) amplitude of vibration, (h-m) SVT instantaneous amplitude and (n) SVT overall amplitude by FFT, and (o-t) LVT amplitude.

In order to examine the detectability of LDRs by vibrothermography, their instantaneous thermal signature during the sweep excitation is inspected. SVT is performed using the same sweep signal used for the SLDV experiment (f = 1-250 kHz, and V_{pp} = 150 V). The linear sweep rate is lowered, leading to a total sweep duration of 50 s. The instantaneous thermal images corresponding to the selected LDR frequencies are presented in Figure 5(h-m) after cold image subtraction. Furthermore, the whole history of sweep excitation is post-processed by FFT in order to obtain an overall amplitude image for the sweep as shown in Figure 5(n). The amplitude images

corresponding to LVT at the same frequencies are shown in Figure 5(o-t) for comparison.

The instantaneous SVT images explicitly show the presence of the BVID at the arbitrary frequency of 95 kHz and at the various LDR_{XY}. There is no indication of the BVID at the fundamental LDR_Z. The observed thermal signature at the arbitrary frequency of 95 kHz is found to be related to the neighboring LDR_{XY} at frequency 91.3 kHz through thermal inertia effects induced by the fast rate of the applied sweep. This is also clearly evidenced by the LVT at 95 kHz, in which not a single indication of the BVID is hinted. These results clearly demonstrate the promising detectability of defects through LDR_{XY} in live monitoring of SVT.

By comparing the instantaneous SVT amplitudes of LDRs (Figure 5(i-m)) with the corresponding LVT amplitudes (Figure 5(p-t)), it is obvious that LVT leads to an increased SNR. The fundamental LDR_Z is detected by DTC of 1 DL and the LDR_{XY} are detected by significantly higher DTC of 18, 5.8, 26.8 and 9.5 DL at 91.3, 116, 129 and 137 kHz respectively. Although the SNR of the SVT is lower compared to LVT, it has a clear benefit in experimental approach. Indeed, the LVT results have been obtained in a total time frame of ~4 hours for each inspected sample. This time frame includes (i) performing the SLDV measurement, (ii) selecting the different LDR frequencies, and (iii) finally performing the LVT measurements. While the SVT results have been obtained in only 50 seconds, free from any SLDV measurement.

The average sweep velocity map of SLDV (Figure 5(g)) and overall amplitude of SVT (Figure 5(n)) provide a comprehensive representation of all activated defect features during sweep excitation. However, the overall SVT image is affected by the 3D anisotropic heat diffusion, leading to some overall blurring effect. These activated areas correspond to the two diagonal lobes identified in the relevant C-scan images (Figure 2(k,l)) as shallow delaminations (with the lowest TOF). As discussed earlier in Section 3.1.3, this limitation is the subject of further investigation.

3.2.2 Sweep frequency spectrum

In order to validate the dominant contribution of LDR_{XY} in vibration induced heating, it is essential to have an accurate measure of the actual out-of-plane and in-plane energy deposited into the sample, and the resultant defect resonation, over the entire excitation frequency range. For this purpose, the thermal and vibrational spectra of the sweep excitation are studied as presented in Figure 6. The figure comprises three columns which show temperature (in digital level DL) (a-c), in-plane velocity V_{xy} (d-f) and out-of-plane velocity V_z (g-i) data, respectively. The top row represents the average of DL, V_{xy} and V_z over the sweep period and a region of interest shown by the path AB along the defected area. The middle row shows a curve plot of DL, V_{xy} and V_z versus frequency at the two most activated areas of the defect (D1, D2) and at a reference non-

defected point (B). The bottom row represents a contour map of both temperature (in digital level DL) and velocity amplitudes V_{xy} and V_z as a function of frequency along the path AB. The measured temperature data are smoothened by Savitzky-Golay filter for improved presentation and interpretation of the thermal spectrum.

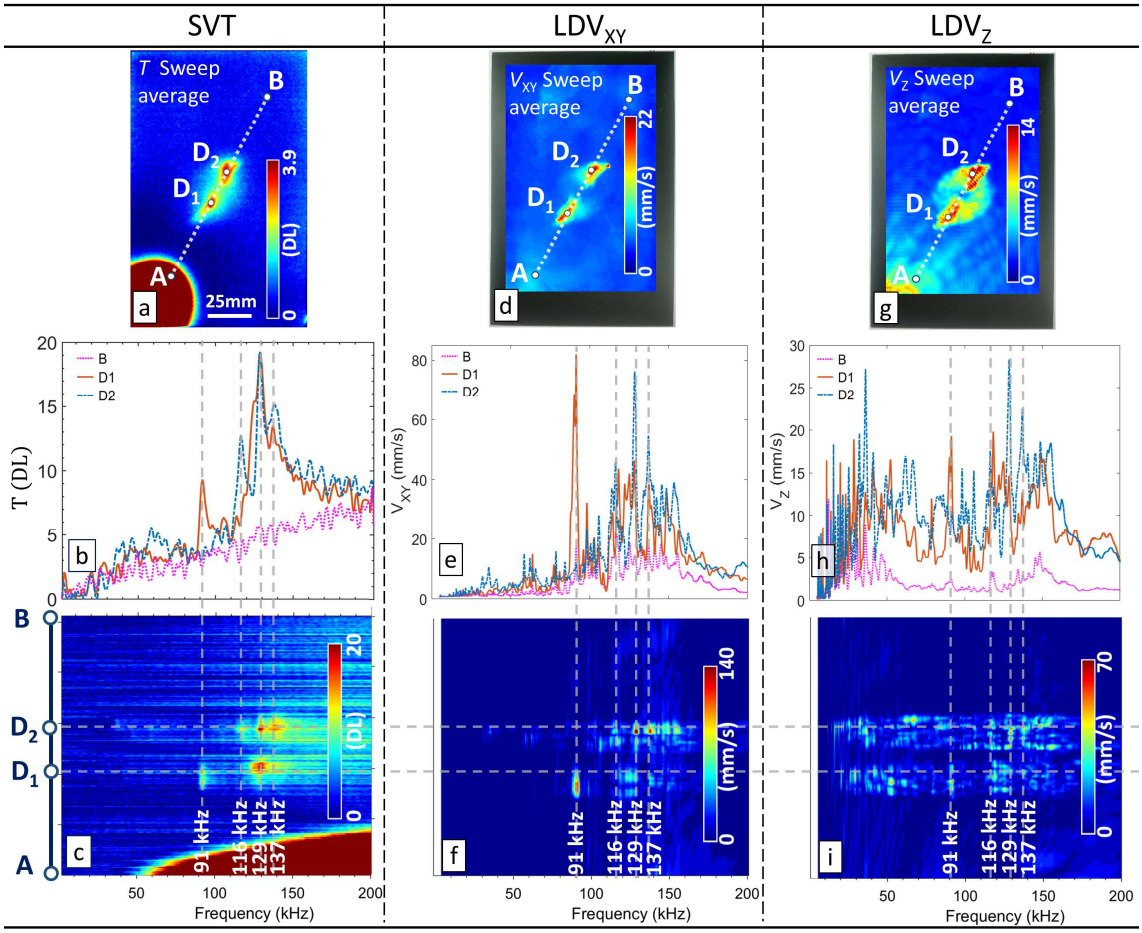

Figure 6. Measurements corresponding to the backside of the quasi-isotropic $[(+45/0/-45/90)]_{3s}$ CFRP sample subjected to a sweep excitation: (a-d) thermal response, (e-g) in-plane vibration amplitude V_{XY}, (h-j) out-of-plane vibration amplitude V_Z.

Figure 6(b) shows the almost steady temperature rise at the non-defected point B and the intensified fluctuating temperature rise at the defected areas D1 and D2 due to LDR phenomena. This is further confirmed by thermal response of the entire path AB as shown in Figure 6(c). At the low frequency range 30-80 kHz, the LDR_Z contributes to slightly higher vibration induced heating of defected area. However, at the higher frequency range 80-150 kHz, significantly higher temperature rise is observed including distinct spikes at LDR_{XY} frequencies as indicated with the dotted vertical lines.

The figures of the in-plane vibrational data (e-f) show that the in-plane velocity V_{xy} reaches distinct local maxima at the same frequencies for which the elevated local heating takes place (see vertical dotted lines). This proves again that this elevated local heating takes place at LDR_{XY} frequencies. The frequencies corresponding to the local

maxima in the thermal and in-plane velocity plots are identical to the four LDR_{XY} frequencies which were manually selected out of the vibrational frequency spectra and used in Figure 5.

Compared to the in-plane velocity V_{xy} (Figure 6 (e,f)), the defected area shows a quite steady elevation of out-of-plane velocity V_z (Figure 6 (h,i)) over the sweep frequency range (due to relatively small wavelength of asymmetric plate modes effective at this low frequency) which is naturally intensified at LDR_Z frequencies. Nonetheless, the heating stages are observed at distinct local maxima of V_{xy} and show minor sensitivity to V_z. Moreover, the elevated amplitude of V_z at LDR_{XY} frequencies is significantly lower than the amplitude of corresponding V_{xy} and has minor effect in vibration induced heating. This is the transversal effect of LDR_{XY} which could be due to the Poisson's effect, possible buckling and rubbing interaction at the in-plane defect interfaces and also projected out-of-plane component of resonation at dominantly in-plane (i.e. slightly oblique) interfaces.

The in-plane velocity V_{xy} and the out-of-plane velocity V_z amplitude curves at the reference point B (see Figure 6(e) and (h)) indicate the ability of the low power piezoelectric actuator to excite the coupon over this broadband frequency range. Desirably, the in-plane excitation is more efficient at the higher frequency range (evidenced by V_{xy} at the reference point B) and the out-of-plane excitation is slightly more efficient at the lower frequency range (evidenced by V_z at the reference point B). This is due to the known behavior of a piezoelectric actuator in stimulation of plate waves, which has better interaction with the wave mode having a wavelength comparable to its size [31]. Therefore, the low frequency LDR_Z and the high frequency LDR_{XY} are adequately stimulated by the attached piezoelectric actuator.

Calculation of the second time (or frequency) derivative of the temperature over frequency sweep excitation, as shown in Figure 7, further quantifies the instantaneous gradient of heating intensity. This provides an exclusive signature of the defects in the absence of the undesirable effects of heating induced by the actuator as well as the thermal trace of LDRs due to thermal inertia. Heating intensity increases in the vicinity of LDR frequencies and has a local minimum value at LDR frequencies as evidenced by red and blue fringes, respectively, in Figure 7(a). This is further clarified by the curves shown in Figure 7(b) corresponding to the defected points D1 and D2 and the non-defected point B where the dips correspond to the four LDR_{XY} frequencies. As such, the SVT shows a great potential to be used for automated extraction of LDR_{XY}.

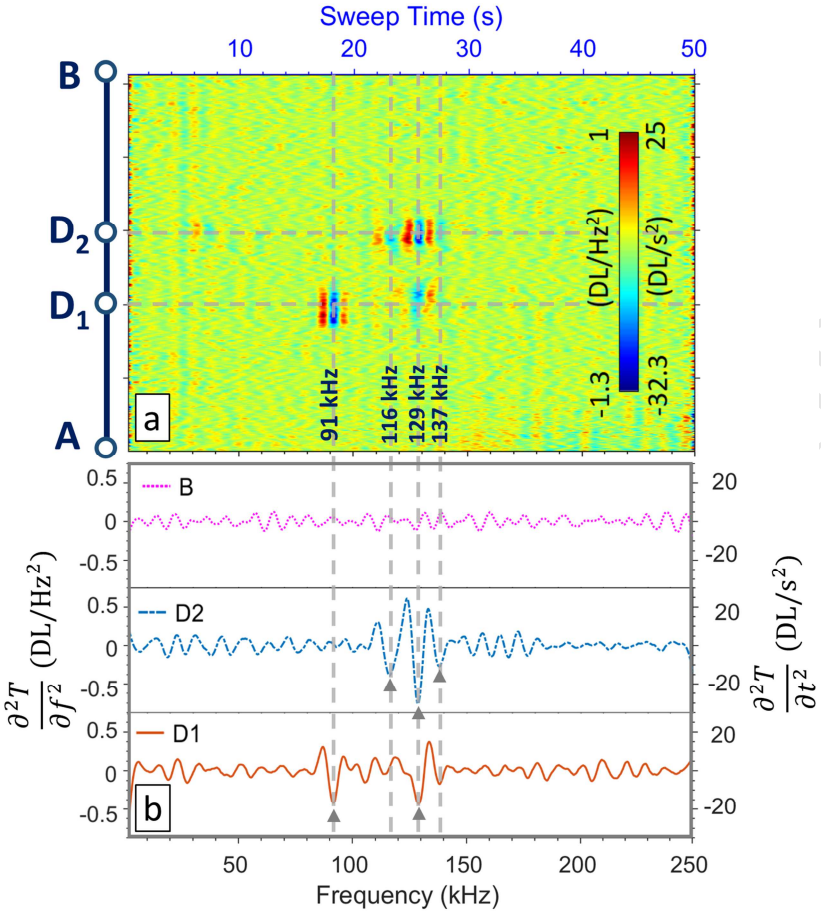

Figure 7. The second time (or frequency) derivative of the thermal response corresponding to SVT of the backside of the quasi-isotropic $[(+45/0/-45/90)]_{3s}$ CFRP sample: (a) over the path AB along the defected area (see Figure 6(a)), (b) at the defected points D_1 and D_2 and the non-defected point B.

3.3 Conclusions

Following the recent extension of classical out-of-plane local defect resonance (LDR) towards in-plane LDR by the current authors, its performance in vibrothermographic NDT is investigated. The combination of in-plane LDR with vibrothermography for highly efficient inspection of BVID in CFRPs has been confirmed. Two CFRP coupons with different lay-up are stimulated with low power piezoelectric excitation, and are inspected using a 3D SLDV and a high sensitivity thermographic camera.

By lock-in vibrothermography, it is shown that the excitation at an in-plane LDR frequency generally results in an increased thermal contrast at the BVID, compared to the excitation at the out-of-plane LDR. This can be explained by the increased in-plane friction of defect interfaces in combination with the higher viscoelastic damping induced by higher in-plane LDR frequencies. The increased heat generation allows to use low power excitation sources.

Moreover, it is shown that due to the highly efficient heat generation at in-plane LDRs, fast sweep vibrothermographic inspection can be performed. In this case, the BVID heating is clearly visible in the live IR amplitude images at each time instance that the excitation frequency corresponds to an in-plane LDR frequency. Thermal and vibrational spectra of the inspection surface are studied and the dominant contribution of in-plane LDR in vibration induced heating is demonstrated. Time-frequency correlation of vibrational and thermal spectra obtained from SVT can be further post-processed for defect quantification and depth profiling.

Acknowledgment

The authors acknowledge Fonds voor Wetenschappelijk Onderzoek Vlaanderen (FWO-Vlaanderen) through grants G0B9515N, 1148018N and 12T5418N. The authors acknowledge the SBO project DETECT-IV (Grant no. 160455), which fits in the SIM research program MacroModelMat (M3) funded by SIM (Strategic Initiative Materials in Flanders) and VLAIO (Flemish government agency Flanders Innovation & Entrepreneurship). The authors express their gratitude towards Honda R&D Co. for supplying material for this research.

References

[1] K. Reifsnider, E. G. Henneke, and W. Stinchcomb, "The mechanics of vibrothermography," in *Mechanics of nondestructive testing*: Springer, 1980, pp. 249-276.

[2] A. Mendioroz, R. Celorrio, and A. Salazar, "Ultrasound excited thermography: An efficient tool for the characterization of vertical cracks," *Measurement Science and Technology,* vol. 28, no. 11, p. 112001, 2017.

[3] K. A. Tsoi and N. Rajic, "Non-destructive evaluation of aircraft structural components and composite materials at DSTO using sonic thermography," DEFENCE SCIENCE AND TECHNOLOGY ORGANISATION VICTORIA (AUSTRALIA) AIR VEHICLES DIV2011.

[4] M. Z. Umar, V. P. Vavilov, H. Abdullah, and A. K. Ariffin, "Detecting low-energy impact damages in carbon-carbon composites by ultrasonic infrared thermography," *Russian Journal of Nondestructive Testing,* journal article vol. 53, no. 7, pp. 530-538, July 01 2017.

[5] A. Katunin, "A Concept of Thermographic Method for Non-Destructive Testing of Polymeric Composite Structures Using Self-Heating Effect," *Sensors,* vol. 18, no. 1, p. 74, 2018.

[6] A. Katunin and D. Wachla, "Analysis of defect detectability in polymeric composites using self-heating based vibrothermography," *Composite Structures,* vol. 201, pp. 760-765, 2018/10/01/ 2018.

[7] I. Solodov and G. Busse, "Resonance ultrasonic thermography: Highly efficient contact and air-coupled remote modes," *Applied Physics Letters,* vol. 102, no. 6, 2013.

[8] I. Solodov, M. Rahammer, D. Derusova, and G. Busse, "Highly-efficient and noncontact vibro-thermography via local defect resonance," *Quantitative InfraRed Thermography Journal,* vol. 12, no. 1, pp. 98-111, 2015.

[9] I. Solodov, D. Derusova, and M. Rahammer, "Thermosonic Chladni figures for defect-selective imaging," *Ultrasonics,* vol. 60, pp. 1-5, 2015/07/01/ 2015.

[10] M. Rahammer, I. Solodov, W. Bisle, D. Scherling, and M. Kreutzbruck, "Thermosonic Testing with Phase Matched Guided Wave Excitation," *Journal of Nondestructive Evaluation,* vol. 35, no. 3, 2016.

[11] G. P. M. Fierro, D. Ginzburg, F. Ciampa, and M. Meo, "Imaging of Barely Visible Impact Damage on a Complex Composite Stiffened Panel Using a Nonlinear Ultrasound Stimulated Thermography Approach," *Journal of Nondestructive Evaluation,* vol. 36, no. 4, 2017.

[12] M. Rahammer and M. Kreutzbruck, "Fourier-transform vibrothermography with frequency sweep excitation utilizing local defect resonances," *NDT and E International,* vol. 86, pp. 83-88, 2017.

[13] D. Dionysopoulos, G. P. M. Fierro, M. Meo, and F. Ciampa, "Imaging of barely visible impact damage on a composite panel using nonlinear wave modulation thermography," *NDT & E International,* 2018.

[14] D. Derusova, V. Vavilov, and N. Druzhinin, "Evaluating impact damage in graphite epoxy composite by using low-power vibrothermography," in *Thermosense: Thermal Infrared Applications XXXVIII*, 2016, vol. 9861, p. 98610F: International Society for Optics and Photonics.

[15] D. Derusova, V. Vavilov, S. Sfarra, F. Sarasini, N. Druzhinin, and V. Nekhoroshev, "Highly efficient ultrasonic vibrothermography for detecting impact damage in hybrid composites," in *Thermosense: Thermal Infrared Applications XXXIX*, 2017, vol. 10214, p. 102140N: International Society for Optics and Photonics.

[16] G. P. M. Fierro, D. Ginzburg, F. Ciampa, and M. Meo, "Nonlinear ultrasonic stimulated thermography for damage assessment in isotropic fatigued structures," *Journal of Sound and Vibration,* vol. 404, pp. 102-115, 2017.

[17] A. Dyrwal, M. Meo, and F. Ciampa, "Nonlinear air-coupled thermosonics for fatigue micro-damage detection and localisation," *NDT & E International,* vol. 97, pp. 59-67, 2018.

[18] G. P. M. Fierro, D. Ginzburg, F. Ciampa, and M. Meo, "Imaging of Barely Visible Impact Damage on a Complex Composite Stiffened Panel Using a Nonlinear Ultrasound Stimulated Thermography Approach," *Journal of Nondestructive Evaluation,* journal article vol. 36, no. 4, p. 69, September 22 2017.

[19] D. Dionysopoulos, G. P. M. Fierro, M. Meo, and F. Ciampa, "Imaging of barely visible impact damage on a composite panel using nonlinear wave modulation thermography," *NDT & E International*.

[20] J. B. Renshaw, *The mechanics of defect detection in vibrothermography*. Iowa State University, 2009.

[21] J. Renshaw, J. C. Chen, S. D. Holland, and R. B. Thompson, "The sources of heat generation in vibrothermography," *NDT & E International,* vol. 44, no. 8, pp. 736-739, 2011.

[22] A. S. Rizi, S. Hedayatrasa, X. Maldague, and T. Vukhanh, "FEM modeling of ultrasonic vibrothermography of a damaged plate and qualitative study of heating mechanisms," *Infrared Physics & Technology,* vol. 61, pp. 101-110, 2013.

[23] J. Segers, M. Kersemans, S. Hedayatrasa, J. Calderon, and W. Van Paepegem, "Towards in-plane local defect resonance for non-destructive testing of polymers and composites," *NDT & E International,* vol. 98, pp. 130-133, 2018.

[24] W. Zhang, S. D. Holland, and J. Renshaw, "Frequency dependence of vibrothermography," in *AIP Conference Proceedings*, 2010, vol. 1211, no. 1, pp. 505-509: AIP.

[25] D. ASTM, "7136/D 7136M-05," *Standard Test Method for Measuring the Damage Resistance of a Fiber-Reinforced Polymer Matrix Composite to a Drop-Weight Impact Event. ASTM International. West Conshohocken PA, USA,* 2005.

[26] S. Spronk *et al.*, "Comparing damage from low-velocity impact and quasi-static indentation in automotive carbon/epoxy and glass/polyamide-6 laminates," *Polymer Testing,* vol. 65, pp. 231-241, 2018.

[27] S. W. F. Spronk *et al.*, "Comparing damage from low-velocity impact and quasi-static indentation in automotive carbon/epoxy and glass/polyamide-6 laminates," *Polymer Testing,* vol. 65, pp. 231-241, 2018/02/01/ 2018.

[28] J. Segers, M. Kersemans, E. Verboven, S. Hedayatrasa, J. Calderon, and W. V. Paepegem, "Investigation to Local Defect Resonance for Non-Destructive Testing of Composites," *Proceedings,* vol. 2, no. 8, 2018.

[29] J. Segers, E. Verboven, S. Hedayatrasa, P. Gaétan, W. Van Paepegem, and M. Kersemans, "Automated extraction of local defect resonance for efficient non-destructive testing of composites," presented at the 9th European Workshop on Structural Health Monitoring, Manchester United Kingdom, 2018.

[30] J. Rantala, D. Wu, and G. Busse, "Amplitude-modulated lock-in vibrothermography for NDE of polymers and composites," *Research in Nondestructive Evaluation,* vol. 7, no. 4, pp. 215-228, 1996.

[31] V. Giurgiutiu, "Lamb wave generation with piezoelectric wafer active sensors for structural health monitoring," in *Smart Structures and Materials 2003: Smart Structures and Integrated Systems*, 2003, vol. 5056, pp. 111-123: International Society for Optics and Photonics.